Climate and human impacts on hydrological processes and flood risk in southern Louisiana

Augusto Getirana*[1,2], Sujay Kumar[1], Goutam Konapala[1,2], Wanshu Nie[1,3], Kim Locke [1,4], Bryant Loomis[5], Charon Birkett[5], Martina Ricko[6], Marc Simard[7]

[1]Hydrological Sciences Laboratory, NASA Goddard Space Flight Center, Greenbelt, MD, USA
[2] Science Applications International Corporation, Greenbelt, MD, USA
[3]Johns Hopkins University, Baltimore, MD, USA
[4]University of Maryland, Earth System Science Interdisciplinary Center, College Park, MD, USA
[5]Geodesy and Geophysics Laboratory, NASA Goddard Space Flight Center, Greenbelt, MD, USA
[6]Kellog Brown & Root (KBR), Columbia, MD, USA
[7]Jet Propulsion Laboratory, Pasadena, CA, USA
*Corresponding author (augusto.getirana@nasa.gov)

Key points

1. Relative impacts of climate-induced hydrological change, water management and sea level rise on Louisiana flooding are quantified
2. Climate-induced hydrological change has increased flood risk over the past 28 years
3. Flood control structures play a vital role in protecting Louisiana's major cities, and in keeping cropland flood-free and productive

Abstract

Satellite observations of coastal Louisiana indicate an overall land loss over recent decades, which could be attributed to climate and human-induced factors, including sea level rise (SLR). Climate-induced hydrological change (CHC) has impacted the way flood control structures are used, altering the spatiotemporal water distribution. Based on "what-if" scenarios, we determine relative impacts of SLR and CHC on increased flood risk over southern Louisiana and examine the role of water management via flood control structures in mitigating flood risk over the region. Our findings show that CHC has increased flood risk over the past 28 years. The number of affected people increases as extreme hydrological events become more exceptional. Water management reduces flood risk to urban areas and croplands, especially during exceptional hydrological events. For example, currently (i.e., 2016-2020 period), CHC-induced flooding puts an additional 73km^2 of cropland under flood risk at least half of the time (median flood event) and 65km^2 once a year (annual flood event), when compared to a past period (1993-1997). A ten- to twenty-fold increase relative to SLR-induced flooding. CHC also increases population vulnerability in southern Louisiana to flooding; additional 9900 residents currently live under flood risk at least half of the time, and that number increases to 27,400 for annual flood events. Residents vulnerable to SLR-induced flooding is lower (6000 and 3300 residents, respectively). Conclusions are that CHC is a major factor that should be accounted for flood resilience and that water management interventions can mitigate risks to human life and activities.

Plain Language Summary

Current scientific literature defines sea level rise as a major factor in increasing global coastal flood risk in recent and future decades, showing that coastal flood risk, particularly over southern Louisiana, is exacerbated by natural and human-induced subsidence. However, the impacts of climate-induced hydrological change (CHC) on flooding and synergy with SLR are often overlooked. Here, we quantify how CHC affect southern Louisiana's water dynamics and its synergy with SLR and water management that results land loss and increase in terrestrial water storage over the decades. We look to answer how much of observed changes are due to CHC and SLR, what are their individual contributions to increasing flood risk, and how local water management contributes to flood resilience.

1. Introduction

River deltas are home to more than half a billion people worldwide, support some of the most productive agricultural land and aquaculture, and their revenue and ecosystem services are conservatively valued at trillions of US dollars (Giosan et al., 2014). Current scientific literature defines sea level rise (SLR) as a major factor in increasing global coastal flood risk in recent and future decades (Oppenheimer et al., 2019; Taherkhani et al., 2020). Coastal flood risk, particularly over deltas, is exacerbated by natural and human-induced subsidence (Kolker et al., 2011; Syvitski et al., 2009), as well as local processes such as wave effects, storm surges, tides, erosion, sedimentation and compaction (Blum & Roberts, 2009; Jankowski et al., 2017; Lam et al., 2018; Olson & Suski, 2021; Oppenheimer et al., 2019; Taherkhani et al., 2020). Although these are all well-known factors affecting the world's deltas, the impacts of climate-induced hydrological change (CHC) on flooding and synergy with SLR are often overlooked. CHC is caused by water cycle intensification due to spatiotemporal changes in water cycle processes (e.g., precipitation and evapotranspiration), resulting in more hydrological extremes. CHC has been detected in many parts of the world (Held & Soden, 2006; Huntington, 2006; Huntington et al., 2018; Ohmura, 2002; Sun et al., 2016; Yeh & Wu, 2018), demonstrating an overall increase in global flood risks in projected 2070-2100 climate scenarios (Hirabayashi et al., 2013). Across the U.S., CHC has motivated discussions about the need to update existing flood control structures (Wright et al., 2019) to build resilience against current and future flood risks. Southern Louisiana has been under climate- and human-induced hydrological pressure for decades. Analysis merging USGS ground measurements with NASA remote sensing and modeled outputs indicates increasing extreme streamflow occurrences in recent years. Monthly upstream inflow [here, upstream inflow is defined as the combination of Mississippi and Red River inflows at the Old River Control Structure (ORCS) – location shown in Figure 1] exceeds the 95th percentile in all five recent years (2016-2020), the same number of extreme flows that occurred over the two prior decades, as shown in Figure 1a. Indeed, river flow is a major factor controlling the lower Mississippi River and its delta water level fluctuations, according to Hiatt et al. (2019). Radar altimetry data derived from the Multi Observation Global Ocean ARMOR3D (Guinehut et al., 2012) shows a clear increase in sea surface heights on coastal Louisiana, with a long-term (1993-2020) positive trend of 2.7mm/year, accelerating in recent years (2002-2020) to 5.1mm/year (Figure 1b). SLR worldwide has been attributed to increasing rates of ice loss from the Greenland and Antarctic ice sheets, as well as sea

temperature increase (Priestley et al., 2021). Terrestrial water storage (TWS) over southern Louisiana also shows a positive trend of 15mm/year over 2002-2020, as estimated by GRACE satellites (Loomis et al., 2019) and shown in Figure 1c. That trend is likely a result of surface water storage increase driven by both climate-induced hydrological changes and SLR. Increasing surface water storage combined with other factors, such as land subsidence, storm surges, and human-induced sediment starvation from dredging, dams, levees, and land management activities have resulted in significant coastal land change since 1988. According to NASA's Delta-X project data (https://deltax.jpl.nasa.gov), coastal Louisiana gained ~1200km^2 over 30 years and lost ~2645km^2, with a net land loss of ~1445km^2 (see Figure 1d). Most of these changes took place within southeastern Louisiana. Recurring hurricane landfall in the region makes southern Louisiana even more vulnerable to coastal erosion, flooding and storm surges. Such a vulnerability to extreme events has motivated major investments in flood prevention since Hurricane Katrina in 2005, improvements which substantially reduced damage in New Orleans during Hurricane Ida in 2021 (Garza, 2021).

Although recent studies coupling atmospheric and coastal circulation models show the synergy of tides, sea level and storm surges controlling extreme flood events on northern U.S. Gulf Coast (Alizad et al., 2018; Bunya et al., 2010; Passeri et al., 2016), knowledge on relative contributions of CHC to southern Louisiana flooding instances is still limited. Motivated by the recent changes over the region described above and the current gap of knowledge on the relative importance of climate-induced hydrological change to flood risks, we quantify the combined and individual impacts of CHC, SLR, and flood control structures (hereafter simply referred to as "water management") on changing flood risk in recent decades. Here, rather than using an ocean-atmosphere coupling approach, we focus on a hydrologic perspective, i.e., we use advanced large-scale hydrological modeling approaches and a simplified representation of ocean dynamics. Such a simplified representation means that satellite-based sea level observations are used as a proxy of ocean dynamics on the coast, compensating for the absence of an ocean model coupled to the hydrological models. The science questions we attempt to answer are: how much of observed trends are due to CHC and SLR; what are their individual contributions to increasing flood risk; and to what extent is water management contributing to flood resilience in southern Louisiana? Here, we refer to southern Louisiana as the domain extending 125-210km inland from the coast, as shown in Fig. 1. This means that it includes not only the coastal zones and wetlands, but also dry lands.

Our advanced hydrological modeling system is composed of two state-of-the-art models coupled within NASA's Land Information System (LIS; Kumar et al., 2006) modeling framework: the Noah with multi-physics (Noah-MP; Niu et al., 2011) land surface model (LSM) and the Hydrological Modeling and Analysis Platform (HyMAP; Getirana et al., 2012a; Getirana, Peters-Lidard, et al., 2017). The system was improved for this study to account for water management and sea level variability at river outlets. Water management is represented in the system as three major flood control structures operated by the U.S. Army Corps of Engineers (USACE). These structures divert about 30% of the water flowing in the Mississippi River. Two structures divert water to the Atchafalaya River through ORCS and the Morganza Spillway, and one diverts water to Lake Pontchartrain through the Bonnet Carre Spillway (locations are shown in Figure 1). SLR is represented in our modeling system with weekly satellite-based sea surface heights (Guinehut et al., 2012) used as downstream boundary conditions. Daily USGS streamflow observations at seven gauges were used as upstream boundary conditions in an attempt to eliminate hydrological model uncertainties propagated through the river network down to the delta. Gauge locations are shown in Figure 1. The modeling system is fully described in Methods section below.

2. Methods

2.1. HyMAP

HyMAP is a state-of-the-art, globalscale flood model capable of simulating surface water dynamics, including water storage, elevation and discharge in-stream, in rivers and floodplains using the local inertia formulation (De Almeida et al., 2012; Bates et al., 2010; Getirana, Peters-Lidard, et al., 2017). Local inertia solves the full momentum equation of open channel flow and accounts for a more stable and computationally efficient representation of river flow diffusiveness and inertia of large water mass of deep flow, which is essential for a physically-based representation of wetlands, lakes, floodplains, tidal effects and impoundments (Getirana et al., 2020). The Courant–Freidrichs–Levy (CFL) condition is used to determine HyMAP's optimal sub timesteps for numerical stability. Rivers and floodplains interact laterally and have independent flow dynamics, with roughness and geometry derived from land cover characteristics, topography and river parameterization (Getirana et al., 2012b, 2013). Hypsographic curves, i.e., the relationship between water elevation (H) and storage (S) are derived from high resolution

topographic data. In addition to S, the flooded area (A) within a grid cell can also be determined through a relationship with H. As a result, floodplain water extent and storage can be derived from the floodplain water elevation with H×S×A relationships. If the water volume within a grid cell is above zero, the minimum A value corresponds to the river area (river length × river width) and it only increases once the river overflows to floodplains, with the grid area as the maximum value. The H×S×A relationship is derived for each grid cell from a pre-processing step where high resolution topography is upscaled to the model spatial resolution. Water overflows to floodplains when the river channel water height is higher than the bank height. This process is considered instantaneous at each timestep. This means that water surface elevations of the river channel and the floodplain are the same.

Digital elevation model (DEM) accuracy plays an essential role in representing river network and floodplain extent in flat areas (Getirana, Bonnet, & Martinez, 2009; Getirana, Bonnet, Rotunno Filho, et al., 2009). In this study, river network parameters were derived from the Multi-Error-Removed Improved-Terrain (Yamazaki et al., 2017) (MERIT) DEM at 3-arcsec spatial resolution. Over southern Louisiana, MERIT DEM is based on the NASA Shuttle Radar Topography Mission (Farr et al., 2007) (SRTM) processed with successive correction of absolute bias, stripe noise, speckle noise, and tree height bias from using multiple satellite data sets and filtering techniques. As a result, MERIT DEM provides a more reliable representation of floodplains and wetlands than the original RSTM DEM. HyMAP resolves the local inertia formulation unidimensionally (i.e., a unique flow direction is attributed to each grid cell) and does not currently represent bifurcations, which is particularly important over deltas and flat areas(Yamazaki et al., 2014). However, its capability of simulating backwater effects combined with interactions between rivers and floodplains results in a pseudo two-dimensional representation of surface water dynamics (Getirana et al., 2021). HyMAP has been extensively evaluated in the Amazon basin (Getirana et al., 2013; Getirana & Peters-Lidard, 2013) and adopted as a tool for regional (Getirana et al., 2014; Jung et al., 2017; Kumar et al., 2016; 2015) and global (Getirana, Kumar, et al., 2017) water cycle studies.

2.2. Noah-MP

The Noah with Multi-Parameterization (Noah-MP; Niu et al., 2011) LSM is used to simulate the vertical water and energy balances over the domain. The Noah-MP LSM builds upon the well-

known Noah LSM (Ek et al., 2003), which has been used in a variety of operational models, applications and research studies. Noah-MP contains four soil layers totaling two meters down the land surface and different parameterization and physics options, which include different static vegetation and dynamic vegetation schemes, canopy resistance effects, radiation transfer, runoff and groundwater schemes, snow model options, and even crop and urban canopy schemes. We apply the prescribed vegetation scheme, based on monthly leaf area index climatology. The TOPMODEL simulated groundwater scheme (Niu et al., 2007) is selected, and the Noah-based lower boundary of soil temperature option is applied. Other climatology-based vegetation and albedo parameter maps include monthly greenness fraction and global (snow-free) albedo (Csiszar & Gutman, 1999).

2.3. HyMAP improvements and customization

Three major improvements and customizations were required to represent the complex surface water processes dominating this domain more accurately in HyMAP. They are (i) the use of a ground-based dataset for the determination of river geometry, (ii) the use of observed streamflow and SSH as upstream and downstream boundary conditions, and (iii) the implementation and customization of a water management module. These features are described below.

2.3.1. River geometry

River geometry parameters used in large-scale river routing schemes are commonly derived from empirical equations (Decharme et al., 2010; Getirana, Kumar, et al., 2017; Li et al., 2015). Such equations are based on generalized representations of world rivers, and their accuracy largely varies from a region to another. Here, in order to minimize errors related to model parameterization, river width and height were derived from the USGS channel measurement network (USGS, 2021). USGS archives ground-based measurements of river width, W_r [m], height, H_r [m], and cross-sectional area, A_r [m^2], at ~31,100 gauges across the country (see Figure SI1a for countrywide data, and Figure SI1b for a zoom over the study domain), totaling approximately 4.4 million river cross-sectional records. A methodology was developed to convert point-based cross-sectional records across the country to spatially distributed river width and height and is described in the Appendix A1.

2.3.2. River boundary conditions

The model was constrained upstream the ORCS structures through direct insertion of streamflow data, at USGS gauges over the Mississippi, Red and Quachita Rivers, where observations are available (see Figure 1 for gauge locations). Directly inserting streamflow observations was performed to reduce uncertainty related to meteorological forcings, model parameterization and numerical representation of physical processes upstream the domain. Temporal data availability varies from one location to another. Outputs from a model run over the entire Mississippi basin composed of HyMAP and Noah-MP at 0.1° spatial resolution and 15-min timestep forced with MERRA-2 meteorological dataset were used to fill the periods without observations. Streamflow simulation errors at gauge locations were minimized by correcting them for bias, lag and standard deviation using the overlapping period with observations as the reference. Hence, the final streamflow time series used as upstream boundary conditions at gauges is a combination of observations and optimized model outputs.

Coastal flooding was represented in the modeling system using sea levels as downstream boundary conditions as a proxy for ocean dynamics. Weekly satellite-based SSH estimates across coastal Louisiana were extracted for the 1993-2020 period from the Multi Observation Global Ocean ARMOR3D (Guinehut et al., 2012). By considering variable SSH in conjunction with the local inertia formulation, as described above, HyMAP can represent coastal backwater flooding, occurring when sea levels are above river levels. This means that water availability in the ocean is assumed unlimited and sufficient to flow inland whenever the model computes inflow (i.e., water flow from the ocean to land/river). For example, in situations where SSH is above river outlet levels, the model will reproduce the backwater effect, resulting in negative river flows. The downside of using weekly SSH is the absence of sub-daily ocean dynamics, including tides.

2.3.3. Water management

HyMAP's water management module was implemented in the framework of this study. Water management is defined here as a human-controlled water diversion from a water body to another. Note that reservoir operation is excluded from this definition of water management, as it is represented in an independent module in HyMAP (Getirana et al., 2020). The water management module requires grid points for the water source (i.e., water body where structures are located) and destination (i.e., nearest water body where water is transferred to) as well as the operation rules.

Three major water management structures are represented in the modeling system: the Old River Control structures (ORCS), the Morganza Floodway (MF) and the Bonnet Carre Spillway (BCS). These structures are operated by USACE and are used for flood control in the lower Mississippi River. Their locations are shown in Figure 1. Numerous other engineered structures exist in the domain, such as levees and small water transfers, and they were neglected in this study due to (i) the lack of representative data, (ii) incompatible scales with model spatial resolution, or (iii) small impact on the regional hydrology. Water management rules at the three selected structures were represented in the modeling system by linear and polynomial equations derived from regressions between reported water diversions and river discharge upstream of management structures, following equations. The representation of flood control structures is fully described in the Appendix A2.

2.4. Model configuration and validation

Noah-MP was driven with NASA's Modern-Era Retrospective analysis for Research and Applications, version 2 (MERRA-2 Reichle et al., 2017) meteorological dataset. Noah-MP and HyMAP are coupled through NASA's Land Information System (LIS; Kumar et al., 2006). These models are one-way coupled, which means that, at each time step, gridded surface runoff and baseflow simulated by Noah-MP are transferred to HyMAP and used to simulate spatially continuous surface water dynamics, but no information is returned from HyMAP to Noah-MP. Model parameters were processed using the Land surface Data Toolkit (LDT; Arsenault et al., 2018) for the domain defined by the coordinates 7.2°W – 2.2°W and 12.1°N – 17.1°N at a 0.02° spatial resolution. Model runs were first spun up for 60 years, allowing the models' water storage components to stabilize, followed by the 1993-2020 period experiments at a 15-minute timestep.

The modeling system accounting for all HyMAP customizations and processes (corresponding to Scenario 4, as described in the following section) was quantitatively evaluated in terms of simulated streamflow and surface water levels at selected locations, as a function of data availability. The accuracy of these variables was quantified through well-known metrics computed using ground-based and satellite observations as references. These metrics are the Kling-Gupta (KG) efficiency coefficient and the normalized root mean square error (NRMSE) between simulations (s) and observations (o). KG measures the Euclidean distance from an ideal point of

the Pareto line and is a function of the correlation (r), bias (β), and standard deviation ratio (γ), also called amplitude ratio, between simulation (s) and observation (o):

$$KG = 1 - \sqrt{(r-1)^2 + (\beta-1)^2 + (\gamma-1)^2} \quad (1)$$

$$\beta = \frac{\mu_s}{\mu_o} \quad (2)$$

$$\gamma = \frac{\sigma_s}{\sigma_o} \quad (3)$$

where μ and σ are the mean and standard deviation of the time series. The optimal value for KG is 1. γ ranges from zero to ∞, where 1 is the optimal value. r ranges from -1 to 1, where 1 is the optimal case. Water levels are bias-corrected before evaluation. As a result, the bias term in KG is neglected. This means that KG for water levels is a function of phasing and amplitude ratio between s and o. NRMSE is defined as follows:

$$\text{NRMSE} = \frac{\left[\sum_{t=1}^{nt}(s_t - o_t)^2/nt\right]^{1/2}}{\sigma_o} \quad (4)$$

where t is the timestep, nt the period length. NRMSE ranges from zero to ∞, where zero is the optimal case.

USGS daily streamflow data is available at 14 gauges monitoring several rivers across the domain, with drainage areas varying from 3474km^2 to 2.96 million km^2. Satellite-based radar altimetry time series of surface water levels were derived from the ESA Sentinel-3A and the multi-agency Jason-2 and Jason-3 satellites at nine locations over the Mississippi and Atchafalaya Rivers. The altimetric dataset is available through the Global Water Monitor (https://blueice.gsfc.nasa.gov/gwm/river/Index).

3. Results

Four "*what-if*" scenarios, listed in Table 1, were designed to distinguish the impacts of CHC, SLR, and water management and quantify their individual and synergetic contributions to southern Louisiana flood risk. In Scenario 1 (or S1), CHC is fully isolated by assuming a constant sea surface height (SSH) at 0.26cm, corresponding to the median of the monthly climatology, with no water management. Scenario 2 (S2) is similar to S1, except that a constant SSH is replaced with a climatology of lower monthly terciles, representing a scenario where CHC co-exists with a seasonal SSH change and no water management. Scenario 3 (S3) replaces SSH climatology with weekly observations to represent climate induced SLR. Scenario 4 (S4) accounts for all three

factors under analysis (i.e., CHC, SLR, and water management), representing the integrated climate and human-induced change and variability. Note that dam operations upstream of the domain are accounted for in all scenarios, since observed streamflow is used as an upstream boundary condition in the modeling system. All four scenarios were simulated over the 1993-2020 period.

Individual and integrated climate and human-induced impacts on southern Louisiana's hydrology are determined as follows:

(i) CHC impacts are isolated in a temporal manner. This means that model outputs of an "early" (1993-1997) period is subtracted from those of a "late" (2016-2020) period, both derived from S1. These model outputs are hereafter referred to $S1_{early}$ and $S1_{late}$, respectively.

(ii) SLR and water management impacts are isolated by subtracting model outputs over the late period from scenarios with and without these factors. This means that SLR impacts are determined as the difference between $S2_{late}$ and $S3_{late}$, and isolated water management impacts are defined as the difference between $S3_{late}$ and $S4_{late}$. The late period was chosen for both factors to better represent recent climate-induced changes on SLR and CHC (the latter directly influences water management).

(iii) Integrated impacts (i.e., all three factors combined) are also determined in a temporal manner by computing the difference between $S4_{early}$ and $S4_{late}$. It is noteworthy that the sum of individual impacts may not total the result derived from all factors combined. This is due to non-linear relationships between different factors and the fact that CHC impacts are computed in a temporal manner, but not SLR or water management impacts.

Such procedures are applied to maps of median (i.e., 50% chance of exceedance for daily events) and annual (i.e., 0.27% chance of exceedance, or $1/365^{th}$) flood events derived for early and late periods of each scenario. Finally, flood risks are quantified in terms of impacts on socioeconomic activities driven by SLR, CHC, water management and all factors combined. Socioeconomic activities are represented here by cropland and population (Center for International Earth Science Information Network - CIESIN - Columbia University, 2018) data. These data were assumed constant throughout the study period as an attempt to isolate climate and human impacts from

regional socioeconomic changes. Nominal years for cropland and population datasets are 2010 and 2020, respectively. Flood risks were quantified by overlapping these data with climate and human-induced changes in median and annual flood events.

3.1. Model evaluation and interpretation

Figure 2 shows the locations and summarizes the model evaluation. Overall efficiency is high across the domain for both streamflow and water levels. Median KG for streamflow is 0.71 and, except for three locations, all values exceed 0.58. Low performance is found at gauges draining small areas. Median KG for water levels is 0.7, with a minimum value of 0.45. Median NRMSE values are 0.04 and 0.13 for streamflow and water levels, respectively. Median amplitude ratio for streamflow is 0.86 and ten locations show values between 0.81 and 1.09, indicating very good agreement. Median γ for water levels is 0.81. Correlation is generally high, with medians of 0.87 for streamflow and 0.84 for water levels. Low performance at some locations can be explained by uncertainties in meteorological forcings and numerical representation of physical processes in the model, as well as model parameterization, particularly river geometry, which can significantly impact water level amplitudes.

Results derived from S4 (i.e., all factors combined) evidence an overall increase in flooded area (Figure 3a) and surface water elevation (Figure 3b) over southern Louisiana. Compared to the early period, the median flooded area increased by ~800km^2 in the late period. This value is lower than Delta-X's estimates as it does not consider other factors, such as land subsidence and human-induced sediment starvation. During the late period, annual events flood an additional ~1700km^2 compared to the early period (not shown). This increase in flooded area is more predominantly observed over the domain's western side and wetlands, but also detected over lower reaches of the Mississippi River, including near New Orleans and coastal areas. On the other hand, a decrease in flooded areas is detected over a plain between the Atchafalaya and Mississippi Rivers. This area is composed of countless small-scale interconnected manmade canals and bayous not represented in our modeling system due to scale restrictions and limited data access, which may result in uncertainties at local scales. Similar patterns are observed in the surface elevation map. More prominent elevation change is detected over major rivers stretches, particularly over the Mississippi River upstream of New Orleans, where median surface water elevations have increased by 1-2 meters since the early 90s. As shown in Figures 3c and 3d, flooded areas and surface water

storage (SWS) have increased at rates of 30km^2/year and 0.07mm/year, respectively, since 1993. Increased trend rates start in 2002 (76km^2/year and 0.12mm/year, respectively) show changes in regional hydrological processes in the past two decades. These model outputs corroborate with previously discussed ground- and satellite-based observations.

3.2. Climate and human-induced impacts on flood events

Figure 4 shows the spatial distribution of individual climate and human-induced impacts on median and annual flood events over southern Louisiana. CHC generally increases the median flooded area over the domain by 296km^2 (Figure 4a). This increase is mostly detected near the southwestern part of the domain and land adjacent to the Mississippi River, including its delta and parts of Baton Rouge and New Orleans. Areas with increased flooding total 809km^2. The drop in flooded extent totals 513km^2 and is mostly detected in parts of the Atchafalaya River basin downstream of ORCS. Such a widespread change demonstrates that CHC impacts on flooding are significantly higher than those caused by sea level rise. CHC results in more severe annual flood events in the late period, with a net increase of 1522km^2 of flooded areas for annual events compared to the early period (Figure 4b). Like the median event, most of the increase is detected in the southwestern area of the domain, totaling 2677km^2 of additional flooded areas, with a decrease found in the Atchafalaya River basin and near Lake Pontchartrain, totaling 1155km^2 of drier areas. The large increase over the southwestern area is explained by a regional increase in runoff generation in recent years.

As shown in Figure 4c, compared to the early period, SLR alone (i.e., no synergy with other factors such as tides, storm surges and land subsidence) currently floods an additional 389km^2 of southern Louisiana's land for at least half of the time. Most of the SLR-induced flooding increase is detected in coastal zones, as expected, particularly over southeastern Louisiana. Such an increase reaches up to 40km inland and is observed in some areas near New Orleans. SLR induces an increase in annual flood events to 399km^2 during 2016-20 (Figure 4d), or an additional 10km^2 compared to median events. Such a small difference between median and annual flood events is due to the use of weekly SSH data as a model input, smoothening out daily and sub-daily extreme events like high tides and storm surges.

Figures 4e and 4f show the spatially distributed impacts of water management on median and annual flood events. Compared to CHC and SLR, management shows a much smaller impact on

379 median floods, with an overall negative balance in flooded area of 23km^2 over the domain. This
380 decrease is mostly detected over the lower Mississippi River downstream of ORCS, totaling
381 94km^2. Water management increases flooding over the surroundings of the Atchafalaya River by
382 71km^2. Under annual flood events, water management impacts are significantly more pronounced,
383 further decreasing floods along the lower Mississippi, particularly around urban areas such as
384 Baton Rouge and New Orleans, but also at its delta. Flooding decrease under annual events totals
385 1055km^2 and is counterbalanced with an increase of 462km^2, mostly detected over the Atchafalaya
386 River basin because of significant water transfer from one river to another through ORCS and the
387 Morganza Floodway. Flood increases are also noticed at the Bonnet Carre Spillway and the
388 surroundings of Lake Pontchartrain as a result of the spillway's frequent use during extreme floods
389 in recent years (USACE, 2021).

390 Figure 5 summarizes how different climate and human factors contribute to southern Louisiana's
391 flood risk. CHC-induced flooding currently puts an additional 73km^2 of cropland under flood risk
392 at least half of the time (median flood event) and 65km^2 once a year (annual flood event), compared
393 to the early period. That is a ten- to twenty-fold increase relative to SLR-induced flooding (7km^2
394 and 3km^2, respectively), which is mostly detected over coastal zones. CHC also increases
395 population vulnerability to flooding; compared to the early period, additional 9900 residents
396 currently live under flood risk at least half of the time, and that number increases to 27,400 for
397 annual flood events. The number of residents vulnerable to SLR-induced flood risk is lower (6000
398 and 3300 residents, respectively). Such a difference is explained by (i) the larger flooded area
399 added by CHC and (ii) the spatial distribution of that flooding. SLR mostly impacts wetlands and
400 their surroundings, not as socioeconomically developed. These results suggest that climate-
401 induced hydrological change is a major driver of flood risk over southern Louisiana. Water
402 management, on the other hand, diverts floodwaters away from population centers such as Baton
403 Rouge and New Orleans, and into the Atchafalaya River, protecting as many as 8600 people during
404 median flood events to 33,000 during annual events. Water management also protects cropland; a
405 total of 13km^2 is protected from median flood events, and 61km^2 from annual events. These results
406 demonstrate that flood control structures play a vital role not only in protecting the people in
407 southern Louisiana, but also in keeping a significant area of cropland flood-free and productive.

408 **Discussion**

Sea level rise, combined with factors such as storm surges, tides and land subsidence, is typically assumed to be the main cause of coastal flood risk increase. However, other factors such as climate-induced hydrological change, are often overlooked. Motivated by major hydrological changes over southern Louisiana in recent decades, and based on an advanced modeling system, this study quantified the individual impacts of climate and human factors on regional water dynamics. Our main findings are that (i) CHC is an important factor contributing to flooding and likely poses a large risk to life and property, (ii) SLR impacts alone are limited to coastal zones, and that (iii) water management is key to reducing flood risk over the domain, particularly protecting its cropland and major cities, including as Baton Rouge and New Orleans.

Our modeling system has a pioneering combination of features representing natural and anthropogenic processes, reducing hydrological model uncertainties in coastal areas. However, known limitations may still contribute to uncertain simulations. Typical sources of uncertainty in hydrological modeling are meteorological forcings, numerical representations of physical processes and model parameterizations. Proposed model improvements focused on the latter two. Although impacts of major flood control structures are represented in our model, local-scale flood protection structures, such as those found in New Orleans, were neglected mostly due to spatial scale and limited data availability. As a result, model simulations may have overestimated the number of residents vulnerable to flooding in experiments accounting for water management. This means that the actual number of residents protected by human intervention could be significantly higher than our estimates.

Understanding model limitations is essential when interpreting its outputs and using them for flood resilience and decision-making. Other human interventions, such as irrigation and drainage systems, are also neglected in our modeling system, and could result in uncertain vertical water budget over cultivated areas. Neglecting daily and sub-daily coastal processes, such as high tides and storm surges may have underestimated SLR-induced annual flood events. Hence, we acknowledge that using satellite-based sea level observations as a proxy for ocean dynamics is a limitation and may be a source of uncertainty. A possible solution for that limitation would be a proper ocean-land model coupling, which is beyond the scope of this paper, but recommended for future studies. It is also known that flood modeling is highly sensitive to the numerical representation of river-floodplain dynamics (Getirana et al., 2021; Getirana, Peters-Lidard, et al., 2017; Li et al., 2015; Luo et al., 2017) and river geometry parameterization (Decharme et al., 2012; Getirana et

al., 2013; Yamazaki et al., 2011). Our model was parameterized with refined ground-based measurements of river geometry combined with an advanced global topography dataset, and is capable of numerically representing backwater effects, which is essential for modeling coasts, lakes and wetlands. Indeed, streamflow and water level simulations have overall high performance, as shown in Figure 2. However, we acknowledge that uncertainties remain, and could result in inconsistent river overflow, directly impacting spatiotemporal distribution of flooding.

Our findings demonstrate the usefulness of the modeling system to quantify and understand natural and anthropogenic factors changing southern Louisiana's water dynamics and could be used to evaluate projected impacts. The inclusion of missing physical processes would reduce model uncertainty and further enhance the system, and possibly change our conclusions.

Although our investigation was limited to southern Louisiana, our findings have implications over the world's densely populated and managed coastal areas. It is estimated that 630 million people are vulnerable to projected SLR-induced coastal floods alone (Kulp & Strauss, 2019). Mega-deltas, such as the Ganges-Brahmaputra-Meghna, Nile, Pearl and Mekong River deltas are particularly vulnerable. The Pearl River Delta, for example, witnessed rapid economic development and population rise. Others, such as the Ganges-Brahmaputra-Meghna Delta, in addition to the dense Bangladeshi population, is not equipped with appropriate flood control structures, resulting in frequent coastal flooding. This is, indeed, the case of many locations in developing countries. The scientific community has been gathering and refining information on SLR impacts on these regions, but CHC impacts and its synergy with other climate and human factors are poorly documented. Hence, it is strongly recommended that individual and synergistic impacts of climate and human-induced factors, including but not limited to those considered in this study, be further investigated globally. Such investigations could support the decision-making process on climate-induced migration and relocation, as well as the optimal spatial distribution of flood control structures and water management practices.

Acknowledgements

This research was supported by funding from NASA Headquarters for the Earth Information System (EIS) project. Computing resources supporting this work were provided by the NASA High-End Computing (HEC) Program through the NASA Center for Climate Simulation (NCCS) at NASA Goddard Space Flight Center.

Appendix

A1. Methodology to convert from point-based to grid-based river geometry data

The methodology is composed of three steps, as described below.

Step 1: Definition of representative point-based channel geometry

The number of measurements at USGS gauges varies from one to over one thousand, depending on the location. Channel measurements acquired at a given location vary over time as a function of numerous factors, such as hydrological season, water flow regime, sedimentation, and measurement technique. In this sense, we first need to define representative W_r, H_r and A_r values for all gauges. It is important to note that channel geometry is represented here by rectangular cross sections and large width-to-depth ratio. At gauges with ten or more records, representative values are defined as the top quintile for W_r and A_r, as an attempt to avoid measurements during floods when rivers overflow to floodplains and levees. Representative H_r values at gauges are defined as the highest record. For gauges with no valid river height record, H_r is computed as A_r / W_r. At the end of this step, we have a list of gauges with their respective coordinates, drainage areas and representative channel geometry parameters.

Step 2: Generation of spatially distributed channel geometry map

We used the MERIT-Hydro dataset (Yamazaki et al., 2019) as the baseline to spatialize USGS point-based channel geometry parameters. Among other parameters, MERIT-Hydro includes a gridded 3-arcsec global river flow directions and drainage area maps derived from the MERIT DEM. First, we attributed W_r and A_r values to MERIT-Hydro grid points with matching gauge coordinates and drainage areas. Then, channel geometry at outlets and headwaters were empirically defined. For catchments with at least two data grid points, we used the most downstream point to determine outlet width, W_{outlet} [m], and height, H_{outlet} [m], by assuming these parameters are constant between these two grid points. For catchments with one or no data grid point, W_{outlet} and H_{outlet} were determined through power law relationships with drainage area, A_d [km^2]. These relationships are defined as follows:

$$H_{outlet} = 0.265 \cdot A_d^{0.274} \quad \text{(A5)}$$

$$W_{outlet} = 0.468 \cdot A_d^{0.656} \quad \text{(A6)}$$

For example, W_{outlet} and H_{outlet} for a hypothetical 1000-km^2 catchment would be 1.8m and 43.5m, respectively. Note that, as most U.S. basins are sufficiently well monitored, these equations are only applied to a limited number of small and poorly equipped catchments.

A minimum river width, W_{min} [m], was used at headwater grid points, defined as follows

$$W_{min} = max\left(90 \cdot L_p^{1.585}, 0.01\right) \quad \text{(A7)}$$

where L_p stands for the model spatial resolution in degrees.

The final product of Step 2, is a 3-arcsec spatial resolution river geometry map for the whole U.S.

Step 3: River geometry upscaling

3-arcsec maps were upscaled to 0.02° using the Flexible Location of Waterways (FLOW) method (Yamazaki et al., 2009). Figures A1c and A1d show upscaled H_r and W_r over the domain. River channel roughness coefficients vary as a function of H_r, (for example, values are ~0.03 and ~0.04 over the Mississippi and Atchafalaya Rivers, respectively; roughness increases to 0.08-0.1 over small and shallow tributaries). Figure A1e shows a map of river channel roughness coefficients over the domain. Floodplain roughness is spatially distributed as a function of vegetation types derived from a static map(Masson et al., 2003), where high values correspond to dense vegetated areas and low values to sparser vegetated regions. See Getirana et al.(Getirana et al., 2012b) for more details on the generation of the floodplain roughness map.

A2. Representation of flood control structures

Old River Control structures

The Old River Control structures (ORCS) consist of several large engineering structures, located 120km upstream of Baton Rouge, that began operation in 1962. ORCS capacity is a 19,820m^3/s and was conceived to distribute flow between the Mississippi and Atchafalaya Rivers, as well as to prevent the Atchafalaya River from capturing the flow of the Mississippi River(USACE, 2021). The water diversion rule at ORCS was empirically determined combining monthly streamflow simulations upstream of the structure, at the Mississippi and Atchafalaya Rivers, and observations downstream the structure, at the Atchafalaya River. A simulation of the naturalized system (i.e., no human impact) using the observation based upstream boundary conditions, as described above,

was first performed to determine the naturalized river flow conditions downstream of ORCS. The diverted water was then determined by the difference between observed and simulated streamflow right downstream of the structures. A relationship between the diverted water at ORCS, Q_{ORCS} [m^3/s] and Mississippi River flow right upstream of the structures, Q_{M1} [m^3/s], can be empirically determined through a linear regression, as shown in Figure A2:

$$Q_{ORCS} = 0.241 Q_{M1} \quad \text{(A8)}$$

Morganza Floodway

The Morganza Floodway (MF) is intended to divert excess floodwater from the Mississippi River into the Atchafalaya River basin. Located 80km upstream of Baton Rouge, its construction was completed in 1954, with a 16,990m^3/s maximum capacity. Since its construction, it has been operated only twice, in 1973 and 2011. Daily water diversion at MF is available for the 2011 flood event(USACE, 2021). During the 45-day operation, one can notice a clear break in the relationship between Mississippi River flow at MF and the diverted water flow to the Atchafalaya River basin, as shown in left plot of Figure A3. That break occurs when the Mississippi River flow reaches 32,000m^3/s, allowing us to empirically define two water management rules using polynomial regressions (i.e., $y = ax^2 + bx + c$):

$$if\ Q_{M2} < 32{,}000;\ Q_{AR} = -6.417 \cdot 10^{-7}\ Q_{M2}^2 + 0.044\ Q_{M2} - 552 \quad \text{(A9)}$$

$$if\ Q_{M2} \geq 32{,}000; Q_{AR} = 11.949 \cdot 10^{-6}\ Q_{M2}^2 - 0.658\ Q_{M2} + 9305 \quad \text{(A10)}$$

Where Q_{M2} and Q_{AR} stand for the Mississippi River flow at MF and the diverted flow to the Atchafalaya River basin, respectively. The MF operation is triggered when Q_{M2} reaches 42,475m^3/s and is interrupted when it drops to 18,500m^3/s.

Bonnet Carre Spillway

The Bonnet Carre Spillway (BCS) was built in 1931 to divert a portion of the Mississippi River's flood flows to Lake Pontchartrain. It is located 53km upstream of New Orleans and its full capacity is 7080m^3/s. Daily water diversion at BCS is made available for five flood events that occurred during the 2016-2020 period (USACE, 2021). The BCS operation largely varies from an event to another, as a function of the flood magnitude and how bays are managed during the flood. Here, the events that occurred in Jan 2016, Mar 2018 and Feb 2019 were used in polynomial regressions combining Mississippi River water flow at BCS with diverted water to Lake Pontchartrain (see

555 Figure A4, plot on the left). Regressions can be further refined by isolating days with ascending
556 and descending flow to represent hysteresis, as shown in middle and right plots of Figure A4.
557 Ascending flows are defined here as values higher than the previous record, and descending flows
558 as values lower than the previous record. As a result, the following operation rule has been defined
559 for BCS:

560 $$if\ Q_{M3} \geq Q_{M3_{t-1}};\ Q_{BC} = 13.21 \cdot 10^{-5} Q_{M3}^2 - 8.427\ Q_{M3} + 134{,}569 \quad \text{(A11)}$$

561 $$if\ Q_{M3} < Q_{M3_{t-1}}; Q_{BC} = -2.1 \cdot 10^{-5} Q_{M3}^2 + 2.084\ Q_{M3} - 43{,}526 \quad \text{(A12)}$$

562 Where Q_{M3} and Q_{BC}, both in m^3/s, stand for the Mississippi River flow at BCS and the water
563 diverted to Lake Pontchartrain, respectively. *t*-1 defines the previous time step. The BCS operation
564 is triggered when Q_{M3} reaches 35,400m^3/s and is interrupted when Q_{M3} drops to 26,500m^3/s.

565 **Data Availability**

566 All data used to develop this study is open access through different institutions. The MERRA-2
567 meteorological data set is distributed by the Goddard Earth Sciences (GES) Data and Information
568 Services Center (DISC;
569 https://search.earthdata.nasa.gov/search?as[platforms][0]=Other%3AModels%3A%3AMERRA-
570 2&fpb0=Other&fpc0=Models&fps0=MERRA-2). Streamflow and river measurement data are
571 made available through the USGS Water Data for the Nation portal
572 (https://nwis.waterdata.usgs.gov/nwis). GRACE data is available on
573 https://doi.org/10.15781/cgq9-nh24. Inland radar altimetry data is made available through the
574 Global Water Monitor portal (https://blueice.gsfc.nasa.gov/gwm/river/Index) and ocean radar
575 altimetry is derived from the Copernicus Marine Service (https://doi.org/10.48670/moi-00148 and
576 https://doi.org/10.48670/moi-00149). Delta-X coastal land gain/loss data is available under request
577 by contacting M. Simard.

578 **Code Availability**

579 LIS and LDT are freely available through https://github.com/NASA-LIS/LISF.

580 **Competing Interests**

581 The authors declare no competing interests.

582 **Author Contributions**

A.G. wrote the paper. A.G., S.K., G.K., W.N., B.L., C.B., M.R. and M.S. analyzed the data. A.G. performed the model runs. A.G. and S.K. interpreted the results. A.G., S.K., K.L., B.L. and C.B. revised the manuscript. A.G. and S.K. designed this study. S.K. supported and supervised this research. All authors reviewed and commented on the paper.

Figure and table legends

Table 1. Factors considered in each of the four proposed "what-if" scenarios.

Figure 1. Southern Louisiana: (a) monthly inflow at the Old River Control Structure (ORCS); (b) annual sea level at the delta; (c) terrestrial water storage (TWS) anomaly within the box defined on the large map over 2002-2020; and (d) coastal land gain and loss over 1988-2018. Circles in (a) indicate periods when inflow is above the 95th percentile or below the 5th percentile during 1993-2020. A positive trend is observed in the annual sea level over the same period in (b), with an increased slope since 2002. Similar trends are observed in TWS since 2002 in (c) and coastal land loss since 1988 in (d).

Figure 2. Daily streamflow and water level evaluation: (a) the Kling-Gupta efficiency coefficient; (b) normalized root mean square error; (c) amplitude ratio; and (d) correlation.

Figure 3. Changes in median (a) flooded area and (b) surface water elevation from 1993-97 to 2016-20 combining all climate and human factors considered in this study (i.e., climate-induced hydrological change, sea level rise and water management). Time series of annual (c) flooded area and (d) surface water storage are also shown.

Figure 4. Changes in flooded areas due to climate-induced hydrological changes (CHC; top row), sea level rise (SLR; middle row), and water management (bottom row) over southern Louisiana. On the left, changes in median flooding; On the right, changes in annual flooding events. Numbers on maps correspond to the net change, and areas with increasing (↑) and decreasing (↓) flooding.

Figure 5. Flood risk over southern Louisiana as a function of return period (median and annual events) due to sea level rise (SLR), climate-induced hydrological change (CHC), water

management and all factors combined (all factors). Risk is quantified by changes in flooded (a) cropland and (b) population over southern Louisiana.

Figure A1. Generation of ground-based river geometry maps: (a) USGS river geometry measurement network; (b) zoom over the study domain; and upscaled (c) river height; (d) river width; and (e) river roughness.

Figure A2. Operation of the Old River Control Structures (ORCS) and its numerical approximation. A linear regression between monthly Mississippi River streamflow upstream of ORCS and the water diverted to the Atchafalaya River was defined and used in the modeling system.

Figure A3. Operation of the Morganza Floodway and its numerical approximation. Polynomial regressions used in the modeling system were defined for observed flows below (plot in the middle) and above (plot on the right) 32,000m^3/s.

Figure A4. Operation of the Bonnet Carre Spillway and its numerical approximation. Polynomial regressions used in the modeling system were defined for ascending (plot in the middle) and descending (plot on the right) observed flows.

632 **Tables and Figures**

633

634 **Table 1**

Scenario	Hydrology	Sea level	Water management
S1	Yes	Constant (0.26cm)	No
S2	Yes	Climatology of lower monthly terciles	No
S3	Yes	Weekly	No
S4	Yes	Weekly	Yes

635

636 **Figure 1**

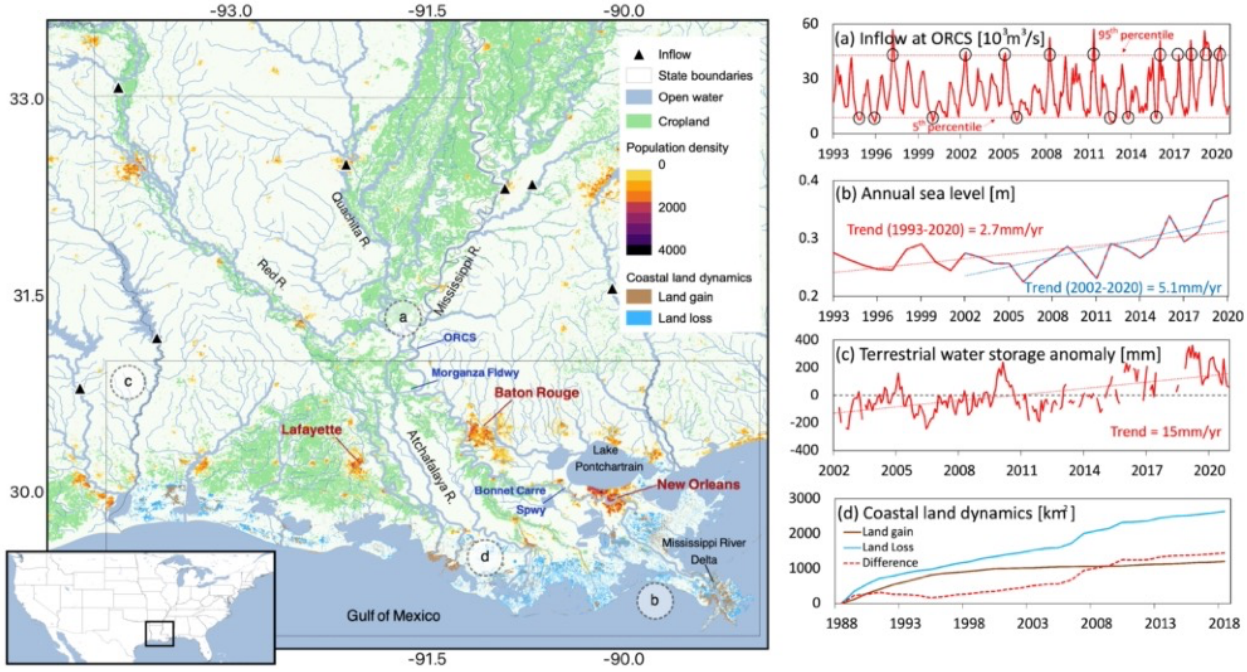

637

638 **Figure 2**

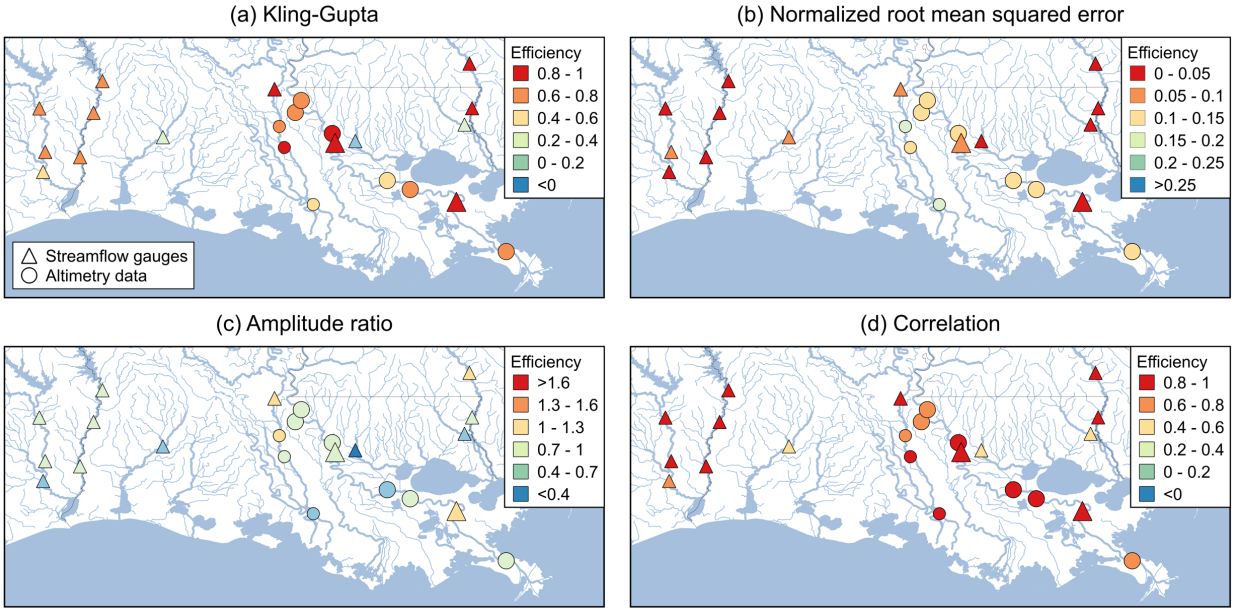

639

Figure 3

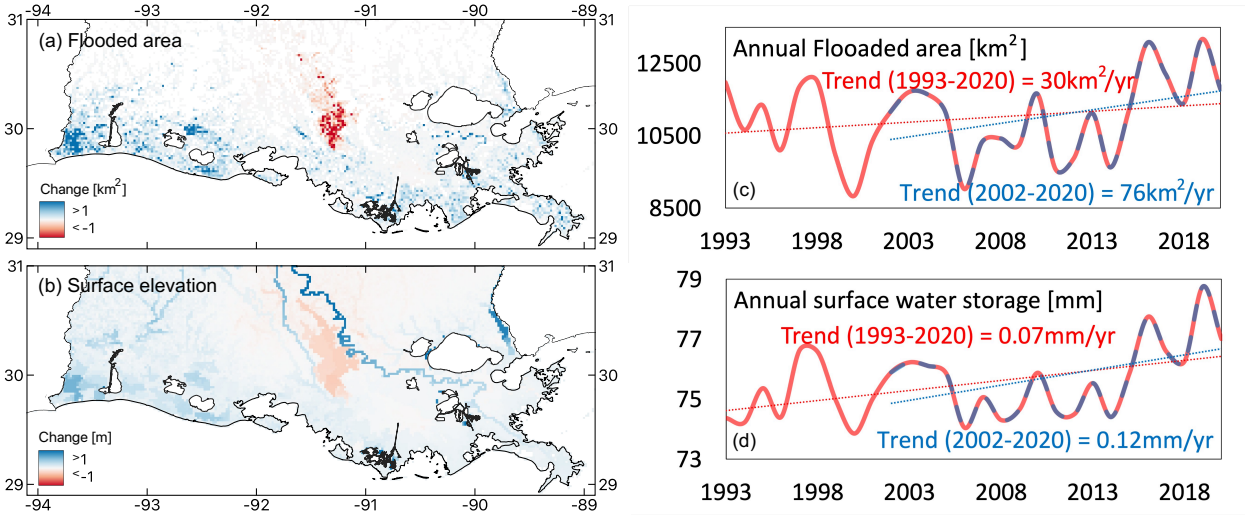
(a) Flooded area
Change [km^2]
>1
<-1
(b) Surface elevation
Change [m]
>1
<-1
-94
-93
-92
-91
-90
-89
31
30
29
Annual Flooaded area [km^2]
Trend (1993-2020) = 30km^2/yr
Trend (2002-2020) = 76km^2/yr
(c)
12500
10500
8500
1993
1998
2003
2008
2013
2018
Annual surface water storage [mm]
Trend (1993-2020) = 0.07mm/yr
Trend (2002-2020) = 0.12mm/yr
(d)
79
77
75
73

642 **Figure 4**

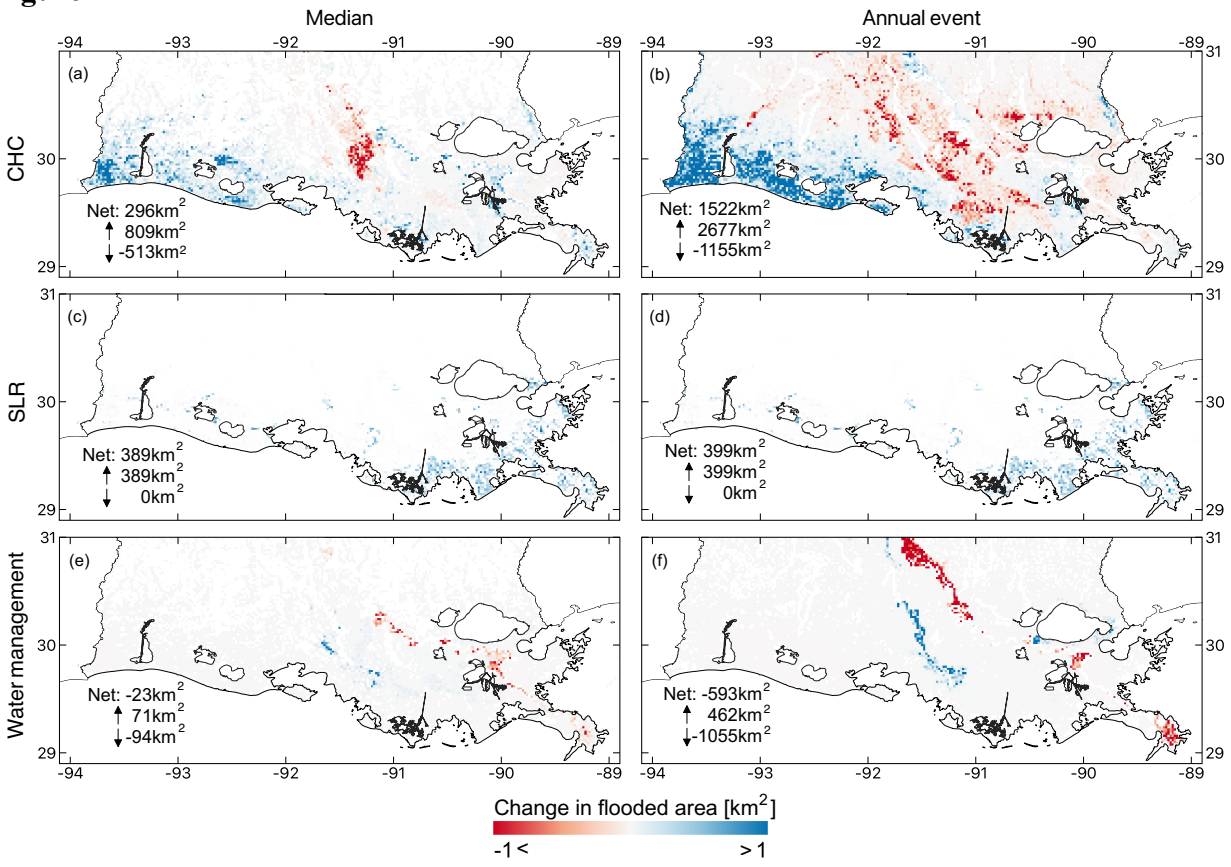

643

644 **Figure 5**

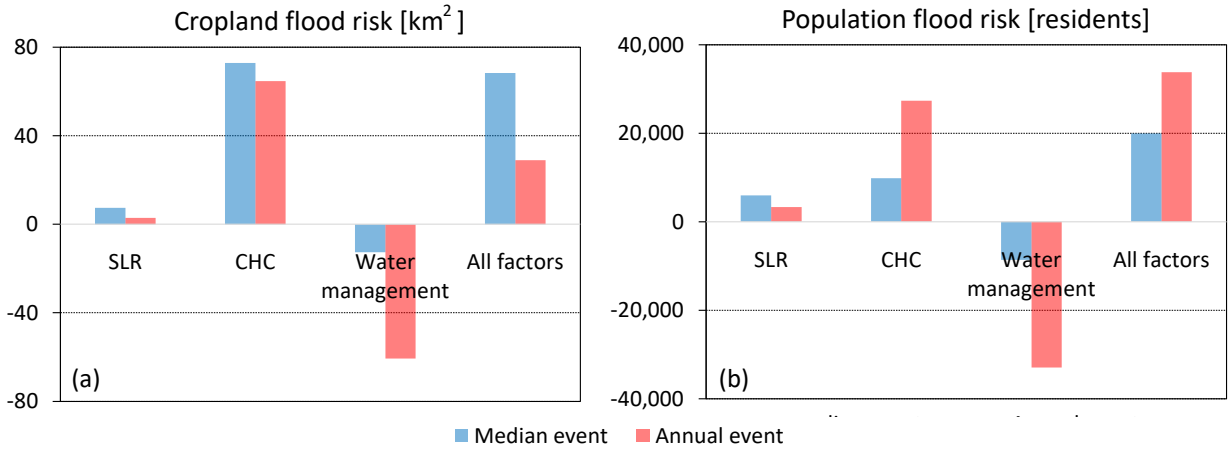

645
646

647 **Figure A1**

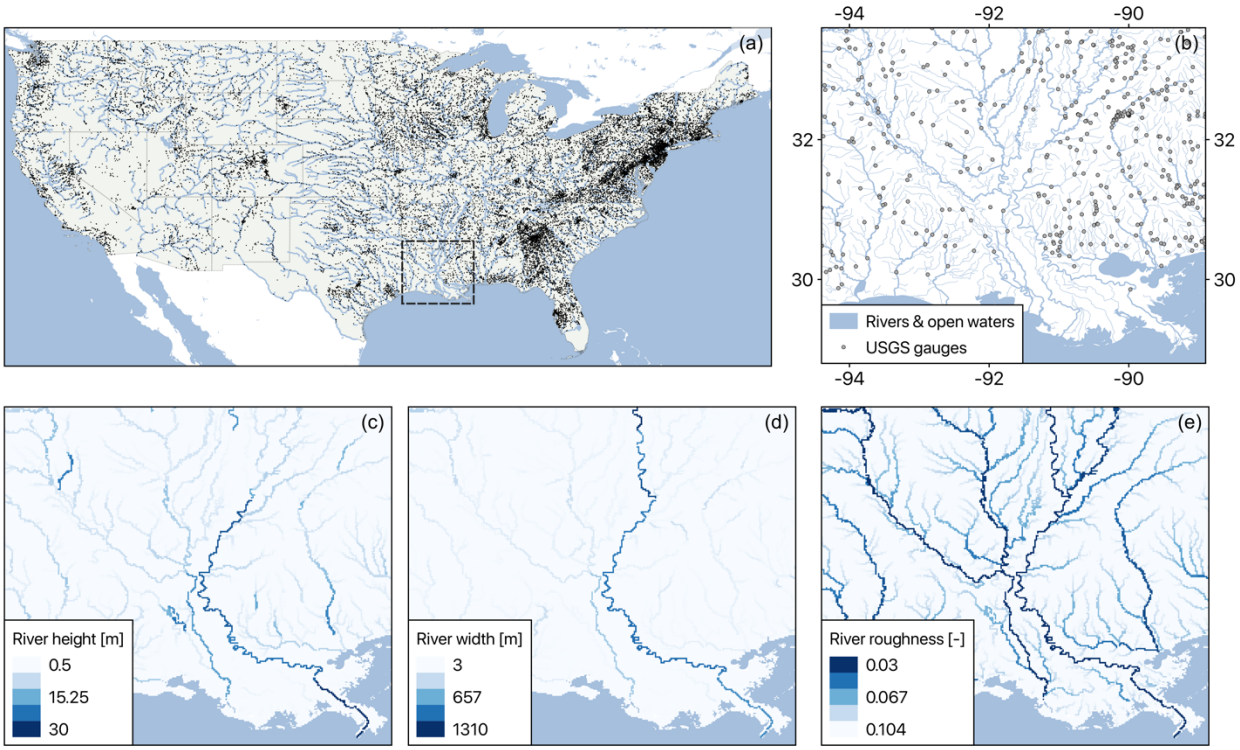

648

649 **Figure A2**

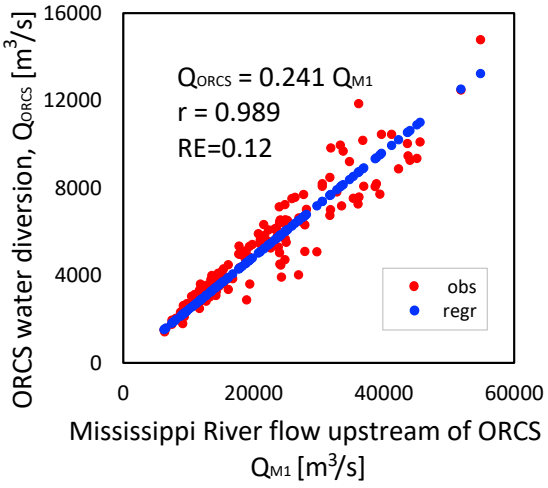

650

Figure A3

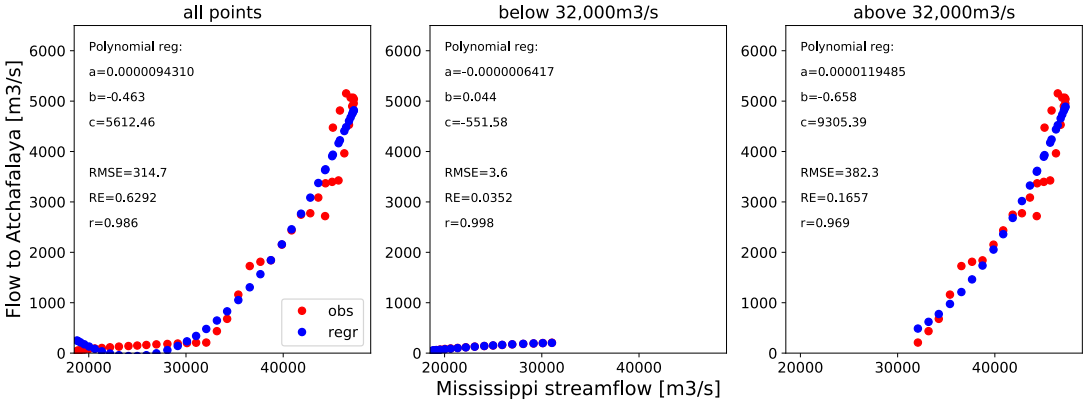
all points
Polynomial reg:
a=0.0000094310
b=-0.463
c=5612.46
RMSE=314.7
RE=0.6292
r=0.986
obs
regr
below 32,000m3/s
Polynomial reg:
a=-0.0000006417
b=0.044
c=-551.58
RMSE=3.6
RE=0.0352
r=0.998
above 32,000m3/s
Polynomial reg:
a=0.0000119485
b=-0.658
c=9305.39
RMSE=382.3
RE=0.1657
r=0.969
Flow to Atchafalaya [m3/s]
Mississippi streamflow [m3/s]

Figure A4

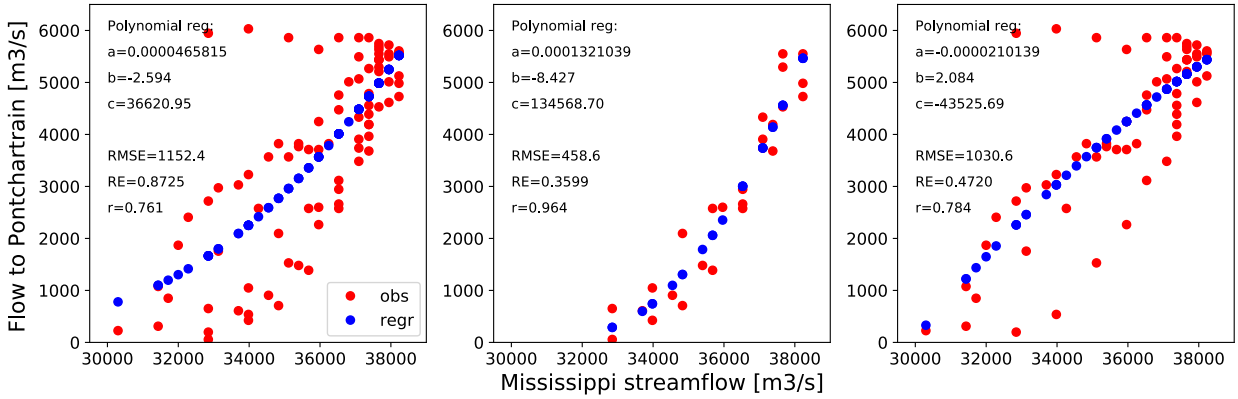
Polynomial reg:
a=0.0000465815
b=-2.594
c=36620.95
RMSE=1152.4
RE=0.8725
r=0.761
obs
regr
Polynomial reg:
a=0.0001321039
b=-8.427
c=134568.70
RMSE=458.6
RE=0.3599
r=0.964
Polynomial reg:
a=-0.0000210139
b=2.084
c=-43525.69
RMSE=1030.6
RE=0.4720
r=0.784
Flow to Pontchartrain [m3/s]
Mississippi streamflow [m3/s]
0
1000
2000
3000
4000
5000
6000
30000
32000
34000
36000
38000

References

Alizad, K., Hagen, S. C., Medeiros, S. C., Bilskie, M. V., Morris, J. T., Balthis, L., & Buckel, C. A. (2018). Dynamic responses and implications to coastal wetlands and the surrounding regions under sea level rise. *PLOS ONE*, *13*(10), e0205176. https://doi.org/10.1371/journal.pone.0205176

De Almeida, G. A. M., Bates, P., Freer, J. E., & Souvignet, M. (2012). Improving the stability of a simple formulation of the shallow water equations for 2-D flood modeling. *Water Resources Research*, *48*(5), 1–14. https://doi.org/10.1029/2011WR011570

Arsenault, K. R., Kumar, S. V., Geiger, J. V., Wang, S., Kemp, E., Mocko, D. M., et al. (2018). The Land surface Data Toolkit (LDT v7.2) - A data fusion environment for land data assimilation systems. *Geoscientific Model Development*, *11*(9), 3605–3621. https://doi.org/10.5194/gmd-11-3605-2018

Bates, P. D., Horritt, M. S., & Fewtrell, T. J. (2010). A simple inertial formulation of the shallow water equations for efficient two-dimensional flood inundation modelling. *Journal of Hydrology*, *387*(1–2), 33–45. https://doi.org/10.1016/j.jhydrol.2010.03.027

Blum, M. D., & Roberts, H. H. (2009). Drowning of the Mississippi Delta due to insufficient sediment supply and global sea-level rise. *Nature Geoscience*, *2*(7), 488–491. https://doi.org/10.1038/ngeo553

Bunya, S., Dietrich, J. C., Westerink, J. J., Ebersole, B. A., Smith, J. M., Atkinson, J. H., et al. (2010). A High-Resolution Coupled Riverine Flow, Tide, Wind, Wind Wave, and Storm Surge Model for Southern Louisiana and Mississippi. Part I: Model Development and Validation. *Monthly Weather Review*, *138*(2), 345–377. https://doi.org/10.1175/2009MWR2906.1

Center for International Earth Science Information Network - CIESIN - Columbia University. (2018). Documentation for the Gridded Population of the World, Version 4 (GPWv4), Revision 11 Data Sets. https://doi.org/https://doi.org/10.7927/H49884ZR

Csiszar, I., & Gutman, G. (1999). Mapping global land surface albedo from NOAA AVHRR. *Journal of Geophysical Research: Atmospheres*, *104*(D6), 6215–6228. https://doi.org/10.1029/1998JD200090

Decharme, B., Alkama, R., Douville, H., Becker, M., & Cazenave, A. (2010). Global evaluation of the ISBA-TRIP continental hydrological system. Part II: Uncertainties in river routing simulation related to flow velocity and groundwater storage. *Journal of Hydrometeorology*, *11*(3), 601–617. https://doi.org/10.1175/2010JHM1212.1

Decharme, B., Alkama, R., Papa, F., Faroux, S., Douville, H., & Prigent, C. (2012). Global off-line evaluation of the ISBA-TRIP flood model. *Climate Dynamics*, *38*(7–8), 1389–1412. https://doi.org/10.1007/s00382-011-1054-9

Ek, M. B., Mitchell, K. E., Lin, Y., Rogers, E., Grunmann, P., Koren, V., et al. (2003). Implementation of Noah land surface model advances in the National Centers for Environmental Prediction operational mesoscale Eta model. *Journal of Geophysical Research: Atmospheres*, *108*(D22). https://doi.org/10.1029/2002JD003296

Farr, T. G., Rosen, P. A., Caro, E., Crippen, R., Duren, R., Hensley, S., et al. (2007). The Shuttle Radar Topography Mission. *Reviews of Geophysics*, *45*(2). https://doi.org/10.1029/2005RG000183

Garza, A. de la. (2021, September). U.S. Civil Engineers Bent the Rules to Give New Orleans Extra Protection from Hurricanes. Those Adjustments Might Have Saved the City During Ida. Retrieved from https://time.com/6094221/hurricane-ida-engineering-protection/

Getirana, A., & Peters-Lidard, C. (2013). Estimating water discharge from large radar altimetry datasets. *Hydrology and Earth System Sciences*, *17*(3). https://doi.org/10.5194/hess-17-923-2013

Getirana, A., Bonnet, M.-P., & Martinez, J.-M. (2009). Evaluating parameter effects in a DEM "burning" process based on land cover data. *Hydrological Processes*, *23*(16). https://doi.org/10.1002/hyp.7303

Getirana, A., Bonnet, M.-P., Rotunno Filho, O. C., & Mansur, W. J. (2009). Improving hydrological information acquisition from DEM processig in floodplains. *Hydrological Processes*, *23*(3). https://doi.org/10.1002/hyp.7167

Getirana, A., Boone, A., Yamazaki, D., Decharme, B., Papa, F., & Mognard, N. (2012a). The hydrological modeling and analysis platform (HyMAP): Evaluation in the Amazon basin. *Journal of Hydrometeorology*, *13*(6). https://doi.org/10.1175/JHM-D-12-021.1

Getirana, A., Boone, A., Yamazaki, D., Decharme, B., Papa, F., & Mognard, N. (2012b). The hydrological modeling and analysis platform (HyMAP): Evaluation in the Amazon basin. *Journal of Hydrometeorology*, *13*(6), 1641–1665. https://doi.org/10.1175/JHM-D-12-021.1

Getirana, A., Boone, A., Yamazaki, D., & Mognard, N. (2013). Automatic parameterization of a flow routing scheme driven by radar altimetry data : Evaluation in the Amazon basin. *Water Resources Research*, *49*(1). https://doi.org/10.1002/wrcr.20077

Getirana, A., Dutra, E., Guimberteau, M., Kam, J., Li, H. Y., Decharme, B., et al. (2014). Water balance in the amazon basin from a land surface model ensemble. *Journal of Hydrometeorology*, *15*(6), 2586–2614. https://doi.org/10.1175/JHM-D-14-0068.1

Getirana, A., Kumar, S., Girotto, M., & Rodell, M. (2017). Rivers and Floodplains as Key Components of Global Terrestrial Water Storage Variability. *Geophysical Research Letters*, *44*(20), 10,359-10,368. https://doi.org/10.1002/2017GL074684

Getirana, A., Peters-Lidard, C., Rodell, M., & Bates, P. D. (2017). Trade-off between cost and accuracy in large-scale surface water dynamic modeling. *Water Resources Research*. https://doi.org/10.1002/2017WR020519

Getirana, A., Jung, H. C., Van Den Hoek, J., & Ndehedehe, C. E. (2020). Hydropower dam operation strongly controls Lake Victoria's freshwater storage variability. *Science of the Total Environment*, *726*, 138343. https://doi.org/10.1016/j.scitotenv.2020.138343

Getirana, A., Kumar, S., Konapala, G., & Ndehedehe, C. E. (2021). Impacts of fully coupling land surface and flood models on the simulation of large wetlands' water dynamics: the case of the Inner Niger Delta. *Journal of Advances in Modeling Earth Systems*. https://doi.org/10.1029/2021MS002463

Giosan, L., Syvitski, J., Constantinescu, S., & Day, J. (2014). Climate change: Protect the world's deltas. *Nature*, *516*(7529), 31–33. https://doi.org/10.1038/516031a

Guinehut, S., Dhomps, A.-L., Larnicol, G., & Le Traon, P.-Y. (2012). High resolution 3-D temperature and salinity fields derived from in situ and satellite observations. *Ocean Science*, *8*(5), 845–857. https://doi.org/10.5194/os-8-845-2012

Held, I. M., & Soden, B. J. (2006). Robust Responses of the Hydrological Cycle to Global Warming. *Journal of Climate*, *19*(21), 5686–5699. https://doi.org/10.1175/JCLI3990.1

Hiatt, M., Snedden, G., Day, J. W., Rohli, R. V., Nyman, J. A., Lane, R., & Sharp, L. A. (2019). Drivers and impacts of water level fluctuations in the Mississippi River delta: Implications for delta restoration. *Estuarine, Coastal and Shelf Science*, *224*, 117–137. https://doi.org/10.1016/j.ecss.2019.04.020

Hirabayashi, Y., Mahendran, R., Koirala, S., Konoshima, L., Yamazaki, D., Watanabe, S., et al. (2013). Global flood risk under climate change. *Nature Climate Change*, *3*(9), 816–821. https://doi.org/10.1038/nclimate1911

Huntington, T. G. (2006). Evidence for intensification of the global water cycle: Review and synthesis. *Journal of Hydrology*, *319*(1–4), 83–95. https://doi.org/10.1016/j.jhydrol.2005.07.003

Huntington, T. G., Weiskel, P. K., Wolock, D. M., & McCabe, G. J. (2018). A new indicator framework for quantifying the intensity of the terrestrial water cycle. *Journal of Hydrology*, *559*, 361–372. https://doi.org/10.1016/j.jhydrol.2018.02.048

Jankowski, K. L., Törnqvist, T. E., & Fernandes, A. M. (2017). Vulnerability of Louisiana's coastal wetlands to present-day rates of relative sea-level rise. *Nature Communications*, *8*(1), 14792. https://doi.org/10.1038/ncomms14792

Jung, H. C., Getirana, A., Policelli, F., McNally, A., Arsenault, K. R., Kumar, S., et al. (2017). Upper Blue Nile basin water budget from a multi-model perspective. *Journal of Hydrology*, *555*, 535–546. https://doi.org/10.1016/j.jhydrol.2017.10.040

Kolker, A. S., Allison, M. A., & Hameed, S. (2011). An evaluation of subsidence rates and sea-level variability in the northern Gulf of Mexico. *Geophysical Research Letters*, *38*(21), n/a-n/a. https://doi.org/10.1029/2011GL049458

Kulp, S. A., & Strauss, B. H. (2019). New elevation data triple estimates of global vulnerability to sea-level rise and coastal flooding. *Nature Communications*, *10*(1), 4844. https://doi.org/10.1038/s41467-019-12808-z

Kumar, S. V., Peters-Lidard, C. D., Tian, Y., Houser, P. R., Geiger, J., Olden, S., et al. (2006). Land information system: An interoperable framework for high resolution land surface modeling. *Environmental Modelling and Software*, *21*(10), 1402–1415. https://doi.org/10.1016/j.envsoft.2005.07.004

Kumar, S. V., Zaitchik, B. F., Peters-Lidard, C. D., Rodell, M., Reichle, R., Li, B., et al. (2016). Assimilation of Gridded GRACE terrestrial water storage estimates in the North American land data assimilation system. *Journal of Hydrometeorology*, *17*(7), 1951–1972. https://doi.org/10.1175/JHM-D-15-0157.1

Kumar, Sujay, Peters-Lidard, C. D., Arsenault, K. R., Getirana, A., Mocko, D., & Liu, Y. (2015). Quantifying the Added Value of Snow Cover Area Observations in Passive Microwave Snow Depth Data Assimilation. *Journal of Hydrometeorology*, *16*(4), 1736–1741. https://doi.org/10.1175/jhm-d-15-0021.1

Lam, N., Xu, Y., Liu, K., Dismukes, D., Reams, M., Pace, R., et al. (2018). Understanding the Mississippi River Delta as a Coupled Natural-Human System: Research Methods, Challenges, and Prospects. *Water*, *10*(8), 1054. https://doi.org/10.3390/w10081054

Li, H.-Y., Leung, L. R., Getirana, A., Huang, M., Wu, H., Xu, Y., et al. (2015). Evaluating global streamflow simulations by a physically based routing model coupled with the community land model. *Journal of Hydrometeorology*, *16*(2). https://doi.org/10.1175/JHM-D-14-0079.1

Loomis, B. D., Luthcke, S. B., & Sabaka, T. J. (2019). Regularization and error characterization of GRACE mascons. *Journal of Geodesy*, *93*(9), 1381–1398. https://doi.org/10.1007/s00190-019-01252-y

Luo, X., Li, H.-Y., Ruby Leung, L., Tesfa, T. K., Getirana, A., Papa, F., & Hess, L. L. (2017). Modeling surface water dynamics in the Amazon Basin using MOSART-Inundation v1.0: Impacts of geomorphological parameters and river flow representation. *Geoscientific Model Development*, *10*(3). https://doi.org/10.5194/gmd-10-1233-2017

Masson, V., Champeaux, J.-L., Chauvin, F., Meriguet, C., & Lacaze, R. (2003). A Global Database of Land Surface Parameters at 1-km Resolution in Meteorological and Climate Models. *Journal of Climate*, *16*(9), 1261–1282. https://doi.org/10.1175/1520-0442-16.9.1261

Niu, G.-Y., Yang, Z.-L., Dickinson, R. E., Gulden, L. E., & Su, H. (2007). Development of a simple groundwater model for use in climate models and evaluation with Gravity Recovery and Climate Experiment data. *Journal of Geophysical Research*, *112*(D7), D07103.

https://doi.org/10.1029/2006JD007522

Niu, G. Y., Yang, Z. L., Mitchell, K. E., Chen, F., Ek, M. B., Barlage, M., et al. (2011). The community Noah land surface model with multiparameterization options (Noah-MP): 1. Model description and evaluation with local-scale measurements. *Journal of Geophysical Research Atmospheres*, *116*(12), 1–19. https://doi.org/10.1029/2010JD015139

Ohmura, A. (2002). CLIMATE CHANGE: Is the Hydrological Cycle Accelerating? *Science*, *298*(5597), 1345–1346. https://doi.org/10.1126/science.1078972

Olson, K. R., & Suski, C. D. (2021). Mississippi River Delta: Land Subsidence and Coastal Erosion. *Open Journal of Soil Science*, *11*(03), 139–163. https://doi.org/10.4236/ojss.2021.113008

Oppenheimer, M., Glavovic, B. C., Hinkel, J., Wal, R. van de, Magnan, A. K., Abd-Elgawad, A., et al. (2019). Sea Level Rise and Implications for Low-Lying Islands, Coasts and Communities. In H.-O. Pörtner, D. C. Roberts, V. Masson-Delmotte, P. Zhai, M. Tignor, E. Poloczanska, et al. (Eds.), *IPCC Special Report on the Ocean and Cryosphere in a Changing Climate*.

Passeri, D. L., Hagen, S. C., Plant, N. G., Bilskie, M. V., Medeiros, S. C., & Alizad, K. (2016). Tidal hydrodynamics under future sea level rise and coastal morphology in the Northern Gulf of Mexico. *Earth's Future*, *4*(5), 159–176. https://doi.org/10.1002/2015EF000332

Priestley, R. K., Heine, Z., & Milfont, T. L. (2021). Public understanding of climate change-related sea-level rise. *PLOS ONE*, *16*(7), e0254348. https://doi.org/10.1371/journal.pone.0254348

Reichle, R. H., Liu, Q., Koster, R. D., Draper, C. S., Mahanama, S. P. P., & Partyka, G. S. (2017). Land Surface Precipitation in MERRA-2. *Journal of Climate*, *30*(5), 1643–1664. https://doi.org/10.1175/JCLI-D-16-0570.1

Sun, S., Sun, G., Cohen, E., McNulty, S. G., Caldwell, P. V., Duan, K., & Zhang, Y. (2016). Projecting water yield and ecosystem productivity across the United States by linking an ecohydrological model to WRF dynamically downscaled climate data. *Hydrology and Earth System Sciences*, *20*(2), 935–952. https://doi.org/10.5194/hess-20-935-2016

Syvitski, J. P. M., Kettner, A. J., Overeem, I., Hutton, E. W. H., Hannon, M. T., Brakenridge, G.

R., et al. (2009). Sinking deltas due to human activities. *Nature Geoscience*, *2*(10), 681–686. https://doi.org/10.1038/ngeo629

Taherkhani, M., Vitousek, S., Barnard, P. L., Frazer, N., Anderson, T. R., & Fletcher, C. H. (2020). Sea-level rise exponentially increases coastal flood frequency. *Scientific Reports*, *10*(1), 6466. https://doi.org/10.1038/s41598-020-62188-4

USACE. (2021). Mississippi River flood control. Retrieved July 7, 2021, from https://www.mvn.usace.army.mil/Missions/Mississippi-River-Flood-Control/

USGS. (2021). Surface Water for USA: Streamflow Measurements. Retrieved from https://nwis.waterdata.usgs.gov/nwis/measurements

Wright, D. B., Bosma, C. D., & Lopez-Cantu, T. (2019). U.S. Hydrologic Design Standards Insufficient Due to Large Increases in Frequency of Rainfall Extremes. *Geophysical Research Letters*, *46*(14), 8144–8153. https://doi.org/10.1029/2019GL083235

Yamazaki, D., Oki, T., & Kanae, S. (2009). Deriving a global river network map and its sub-grid topographic characteristics from a fine-resolution flow direction map. *Hydrology and Earth System Sciences*, *13*(11), 2241–2251. https://doi.org/10.5194/hess-13-2241-2009

Yamazaki, D., Kanae, S., Kim, H., & Oki, T. (2011). A physically based description of floodplain inundation dynamics in a global river routing model. *Water Resources Research*, *47*(4), 1–21. https://doi.org/10.1029/2010WR009726

Yamazaki, D., Sato, T., Kanae, S., Hirabayashi, Y., & Bates, P. D. (2014). Regional flood dynamics in a bifurcating mega delta simulated in a global river model. *Geophysical Research Letters*, *41*(9), 3127–3135. https://doi.org/10.1002/2014GL059744

Yamazaki, D., Ikeshima, D., Tawatari, R., Yamaguchi, T., O'Loughlin, F., Neal, J. C., et al. (2017). A high-accuracy map of global terrain elevations. *Geophysical Research Letters*, *44*(11), 5844–5853. https://doi.org/10.1002/2017GL072874

Yamazaki, D., Ikeshima, D., Sosa, J., Bates, P. D., Allen, G. H., & Pavelsky, T. M. (2019). MERIT Hydro: A High-Resolution Global Hydrography Map Based on Latest Topography Dataset. *Water Resources Research*. https://doi.org/10.1029/2019WR024873

Yeh, P. J. -F., & Wu, C. (2018). Recent Acceleration of the Terrestrial Hydrologic Cycle in the

U.S. Midwest. *Journal of Geophysical Research: Atmospheres*, *123*(6), 2993–3008. https://doi.org/10.1002/2017JD027706